Analyst

ROYAL SOCIETY OF CHEMISTRY

PAPER

View Article Online
View Journal

Cite this: DOI: 10.1039/d0an01870h

The functionalization of gold nanoparticles as a novel platform for the highly efficient electrochemical detection of silver ions

Zhourui Xiao,† Han Meng,† Xuefei Qin, Xueqing Sang, Yun Zhang * and Yali Yuan *

Received 17th September 2020,
Accepted 29th October 2020

DOI: 10.1039/d0an01870h

rsc.li/analyst

Herein, a novel electrochemical biosensor was constructed for the highly efficient detection of silver ions. A porous platform constructed with functionalized gold nanoparticles (AuPP) was electropolymerized on the gold electrode surface. The obtained polymer, analogous to a metal–organic framework, was used as the sensing platform together with cytosine–Ag^+–cytosine interaction for dual signal amplification. The scanning electron microscopy (SEM) image of the AuPP platform exhibited a porous structure and considerable binding sites for C-riched single stranded DNA, leading to predictable silver ion preconcentration. Based on this strategy, the biosensor showed that the peak current in differential pulse voltammetry rose linearly as the concentration of silver ion increased from 0.005 to 3 μM with a detection limit of 1.3 nM. In addition, in the presence of other metal ions, such as Pb^{2+}, Mn^{2+}, Ni^{2+}, Co^{2+}, Cu^{2+}, Zn^{2+}, Na^+, Ca^{2+}, and Cd^{2+}, at the same concentration, the current signal remained almost unchanged, manifesting high selectivity for Ag^+. This proposed sensor might exhibit a novel fabrication method for metal ion detection with the aid of multiple AuPP materials by designing ligands with different functional groups.

1. Introduction

As an important transition element, silver is extensively used in a variety of fields, such as jewellery, cosmetics, pharmaceutical preparations, photography, electronic equipment and catalysis.[1–4] However, substantial research efforts have recently been made to reveal the threats silver ion may lead to for the environment and human health,[5,6] since it can bind to the thiol, amino, and carboxyl groups of functional enzymes and trigger severe disruption to biosystems.[7,8] The safe value of silver in drinking water stipulated by the World Health Organization (WHO) is 0.05 ppm, while the threshold exposure limit of silver in water for fish and microorganisms is set at lower than 1.6 nmol L^{-1}. Therefore, it is of great importance to monitor silver ions in environmental and industrial samples with high selectivity, accuracy and sensitivity.

Among a variety of detection procedures for silver ions, the electrochemical method is a common and extensively applied technique due to its advantages, including inexpensive instrumentation, simple operation, rapidity and ease of on-site application. To achieve the required selectivity and sensitivity, different strategies involving various nanomaterials have been attempted to address the issue.

A primary step to obtain selectivity in the electrochemical method is to confine the detection within a specific potential range, but it is not effective in blocking interferents possessing similar electroactive potentials. Other target-specific receptors should be introduced for precise recognition. Based on the fact that sulfur can form stable bonds with silver and on the mechanism and strength of the Ag–S bond as confirmed by theoretical research,[9,10] sulfur-containing materials, such as sulfur quantum dots (QDs),[11] sulfur-doped graphene,[12] and oxygen and sulfur co-doped graphitic carbon nitride QDs,[13] are used to selectively capture silver ions. However, this interaction may be interrupted by other heavy metals such as Au, Hg, and Cd. Therefore, the most accepted method is based on cytosine (C)–Ag^+–C conjugation,[14] which has satisfactory selectivity to Ag^+ and helped develop electrochemical,[15,16] colorimetric[17] and fluorescence[18,19] methods for various sensing purposes. The application of C-riched oligonucleotides can selectively extract Ag^+ from a complex system; meanwhile, it can also be used as a process of preconcentration, greatly improving the sensing performance.

The main methods for reducing the detection limit, *i.e.* improving sensitivity, usually include introducing signal amplification[20,21] or increasing the active surface area of working electrodes. For signal amplification, the determi-

College of chemistry and bioengineering, Guilin University of Technology, 12 Jiangan Road, Guilin 541004, China. E-mail: thanksin2013@163.com, zy_hnu@163.com
† These two authors contributed equally.

nation in some cases must go through repeated reaction cycles related to enzymes,[21] DNA[22] or multiple substrates,[23] making the process complex and time-consuming, especially when one reaction cycle contains several steps. To simplify the procedure, nanomaterials with different properties and morphologies are emerging as electrochemical signal enhancers and attracting wide research interest.[24–26] In these cases, the nanomaterials not only play the role of signal enhancer, but also increase the specific surface area to a certain extent. Based on this, enlargement of the active surface area is relatively easy to carry out and achieve high sensitivity with the help of diverse nanomaterials, such as GaN micropillars,[27] a platinum/gold nanoarray,[28] CeO_2/g-C_3N_4 nanocomposite[29] and SnO_2 nanoflowers with porous structure.[30] Of the aforementioned materials, gold nanoparticles (Au NPs) have recently received great attention in electrochemical analysis due to their tunable size, good conductivity and ease of surface modification. When functionalized with the appropriate groups using diverse organic ligands, the physicochemical properties of Au NPs can be significantly enhanced, thus expanding the application area of Au NPs. By designing the surface ligands and performing a polyreaction process, the functionalized Au NPs can form a porous network consisting of metal nodes and organic linkers, which may be regarded as an analog of a metal–organic framework (MOF).[31] Such a structure has the benefit of increased accessible active sites, high specific surface area, and fast mass transfer. Taking these merits into account, Au NPs functionalized with electroactive ligands are powerful candidates for the construction of sensing platforms in electrochemical analysis.

Herein, a novel platform constructed from 4-aminothiophenol (4-ATP) modified Au NPs (Au@4-ATP) was introduced for Ag^+ sensing by simple electropolymerization (Scheme 1). After a layer of 4-ATP self-assembled on the gold electrode surface through Au–S bonds, the synthesized Au@4-ATP nanoparticles acted as monomers and linked with each other to form a uniform and porous network under scanning at certain potentials, offering increased active surface area. In the following step of immobilizing C-riched ssDNA, increased active binding sites allowed a considerable loading amount of the DNA chains and thus more C–Ag^+–C mismatch, achieving selective preconcentration of Ag^+. These two sections offered dual signal amplification, fully implementing the sensitive and selective detection of Ag^+.

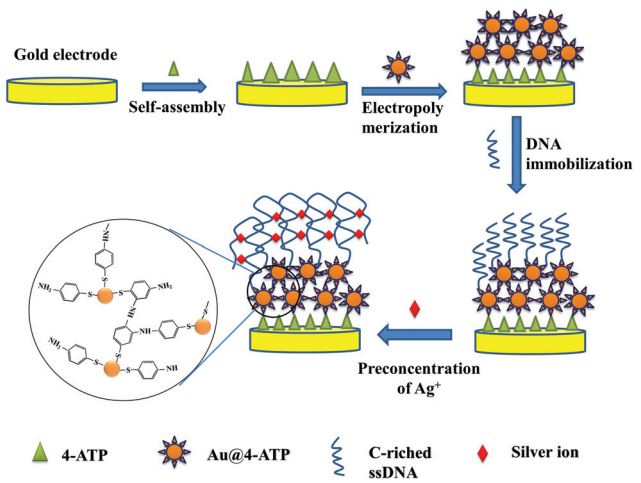

Scheme 1 Schematic illustration of Ag^+ detection principle based on a novel platform constructed with Au@4-ATP.

2. Experimental section

2.1 Reagents and apparatus

Chloroauric acid trihydrate ($HAuCl_4 \cdot 3H_2O$), methanol, and 4-aminothiophenol were purchased from Aladdin Biochem Technology Co. Ltd. Sodium borohydride and sodium acetate were bought from Xilong Scientific Co., Ltd. Silver nitrate was obtained from Sinopharm Chemical Reagent Co., Ltd. C-Riched ssDNA (5′-CCC CCC CCC CCC CCC CCC-3′) was obtained from Sangon Biotechnology (Shanghai) Co., Ltd. Interference metal ion solutions of Pb^{2+}, Mn^{2+}, Ni^{2+}, Co^{2+}, Cu^{2+} and Zn^{2+} were prepared from their respective metal salts. All other chemical reagents were of analytical grade and used without further purification.

Infrared absorption spectra of Au@4-ATP and 4-ATP were recorded on a Nicolet NEXUS 470 Fourier transform-infrared (FT-IR) spectrometer (Nicolet, USA). X-ray photoelectron spectroscopy (XPS) was performed on a Kratos AXIS Hsi spectrometer using a monochromatic Al Kα X-ray source (1486.6 eV). C 1s at 284.6 eV was used as the charge reference to determine core level binding energies. The morphology of Au@4-ATP and the modified gold electrode surface were observed on an S-4800 field emission scanning electron microscope (SEM) (Hitachi, Japan) and a JEOL JEM-2100F transmission electron microscope (TEM), respectively.

Electrochemical measurements were conducted using an electrochemical workstation (CHI 660D, Shanghai Chenhua Instruments, China) with a conventional three-electrode system comprised of a saturated calomel electrode as the reference electrode, a platinum wire as the counter electrode and a modified Au electrode (3 mm diameter) as the working electrode. Electrochemical impedance spectroscopy (EIS) was carried out on an electrochemical workstation (Autolab PGSTAT128N, Metrohm Co., Ltd) in the frequency range of 0.1 Hz to 1 M Hz using 5 mM $K_3[Fe(CN)_6]/K_4[Fe(CN)_6]$ containing 0.1 mol L^{-1} KCl as the electrolyte. The EIS data was simulated using Zview software.

2.2 Synthesis of Au@4-ATP

Au@4-ATP were synthesized through a one-step reduction method as reported in the literature[32] with slight modification. Typically, 31.6 mg (8.1×10^{-6} mol) of $HAuCl_4 \cdot 3H_2O$ dissolved in 30 mL methanol was placed in a 250 mL round-bottom flask. 20.0 mg (3.9×10^{-6} mol) of 4-ATP in 12 mL of a methanol/water (1 : 1 v/v) mixture was added dropwise to the gold salt solution under continuous stirring, with the mixture color

changing slowly from yellow to dark brown. At this point, stirring was stopped and the reaction was allowed to stand for another 10 min. Next, 2.2 mL of freshly prepared 3.6 mM $NaBH_4$ aqueous solution was added dropwise to the obtained brown mixture under vigorous stirring at room temperature. With the addition of $NaBH_4$, the reaction solution became darker, followed by the appearance of black precipitate. After another 10 min of stirring, the solution was kept in the dark for 1 h. The final product was filtered using a 0.22 μm polymer membrane and washed successively with water and ether. The resulting black powder was dried and ready for use.

2.3 Fabrication of porous platform with DNA on the gold electrode surface

Prior to surface modification, the gold electrode was carefully polished with alumina powder and rinsed thoroughly with acetone, ethanol and ultrapurified water in succession. It was then activated in 0.5 mol L^{-1} H_2SO_4 by cyclic voltammetry (CV) in the range of −0.2 V–1.6 V to get a stable curve. The obtained clean gold electrode was immersed in 0.05 mol L^{-1} 4-ATP ethanol solution at 4 °C for 12 h and the fabrication of the porous polymer (AuPP) was then performed by electropolymerization using CV technique in the potential range of 0–0.6 V at 80 mV s^{-1} for 25 cycles in a PBS solution (pH 5.8) containing 0.1 mg mL^{-1} Au@4-ATP. After the construction of AuPP, the DNA was immobilized on the polymer at a potential of +0.5 V for 300 s from a stirred Tris-HCl buffer solution (pH 7.2) containing 1 μmol L^{-1} DNA. In this way, the DNA/AuPP/Au electrode was prepared and dried at room temperature for application in Ag^+ determination.

2.4 Electrochemical measurements

Different concentrations of Ag^+ in 0.10 mol L^{-1} HNO_3 supporting electrolyte were transferred into the electrochemical cell and the working electrode was pretreated at −0.54 V for 350 s to facilitate the accumulation of Ag^+, followed by differential pulse voltammetry (DPV) for the detection process in the potential range of −0.1–0.6 V, with a potential increment of 0.01 V, amplitude of 0.04 V, and pulse width of 0.2 s.

3. Results and discussion

3.1 Characterization of Au@4-ATP and the constructed AuPP platform

IR spectrometry was used to characterize the obtained Au@4-ATP and the results compared with 4-ATP are shown in Fig. 1A (a). The deformation vibration absorption peak of C=C in the backbone of aromatic hydrocarbons appeared around 1620 cm^{-1}, 1592 cm^{-1} and 1422 cm^{-1} for both Au@4-ATP and 4-ATP (shown in red circle). The vibration absorption peak of C–H appearing around 824 cm^{-1} indicated *para*-substitution on the benzene ring. The absorption peaks at around 1270 and 1265 cm^{-1} in Fig. 1A(a) and (b) were both ascribed to the C–N stretching vibration. Based on the IR spectra of 4-ATP and Au@4-ATP, they have similar absorption peaks, with the

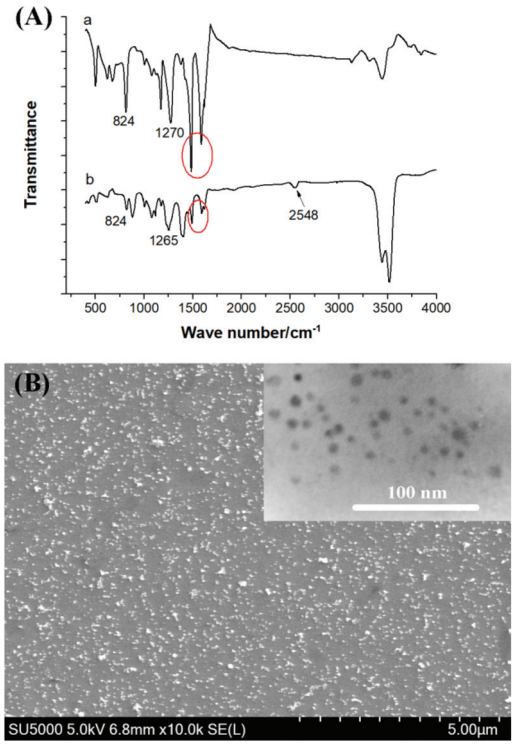

Fig. 1 (A) IR spectra of (a) Au@4-ATP and (b) 4-ATP. (B) SEM image of Au@4-ATP. Inset: TEM image of Au@4-ATP.

obvious exception that the S–H absorption peak of Au@4-ATP (2548 cm^{-1}) entirely vanished, implying the formation of an Au–S bond. The morphology of synthesized Au@4-ATP was characterized by SEM and TEM and the results (Fig. 1B) showed that the Au@4-ATP particles were monodispersed with an average size of around 10 nm, which was consistent with the literature.[32]

Furthermore, XPS was used to confirm the chemical state and surface composition of Au@4-ATP. Fig. 2a exhibits the survey spectrum from 0 to 1350 eV. Besides the Au and C elements, N and S elements can both be observed in the spectrum. Fig. 2(b–d) show the core level spectra of S 2p, N 1s and Au 4f, respectively. The two peaks in Fig. 2b at 163.6 and 162.4 eV correspond to S $2p_{1/2}$ and S $2p_{3/2}$, with a difference in binding energy of 1.2 eV, and have been proven to be the two peaks of S attached to the Au surface.[33] This was consistent with the phenomenon that after the self-assembly of thiol molecules onto the Au surface, the binding energy of S $2p_{3/2}$ shifted lower.[34] In Fig. 2c, the N 1s peak was deconvoluted into two peaks, indicating there were two electronic states of N: the benzenoid amine centered at 399.8 eV and the nitrogen cationic radical ($N^{\bullet+}$) at 401.3 eV.[35] Fig. 2d shows Au 4f binding energy peaks at 87.9 eV (Au $4f_{5/2}$) and 84.2 eV (Au $4f_{7/2}$) corresponding to metallic Au. Compared with bulk Au crystal, 4-ATP passivated Au nanoparticles displayed the higher-binding-energy shift of Au 4f core-level photoemission spectra.[36]

The Au@4-ATP nanoparticles were electropolymerized on the Au electrode by scanning 25 CV cycles in pH 5.8 PBS with

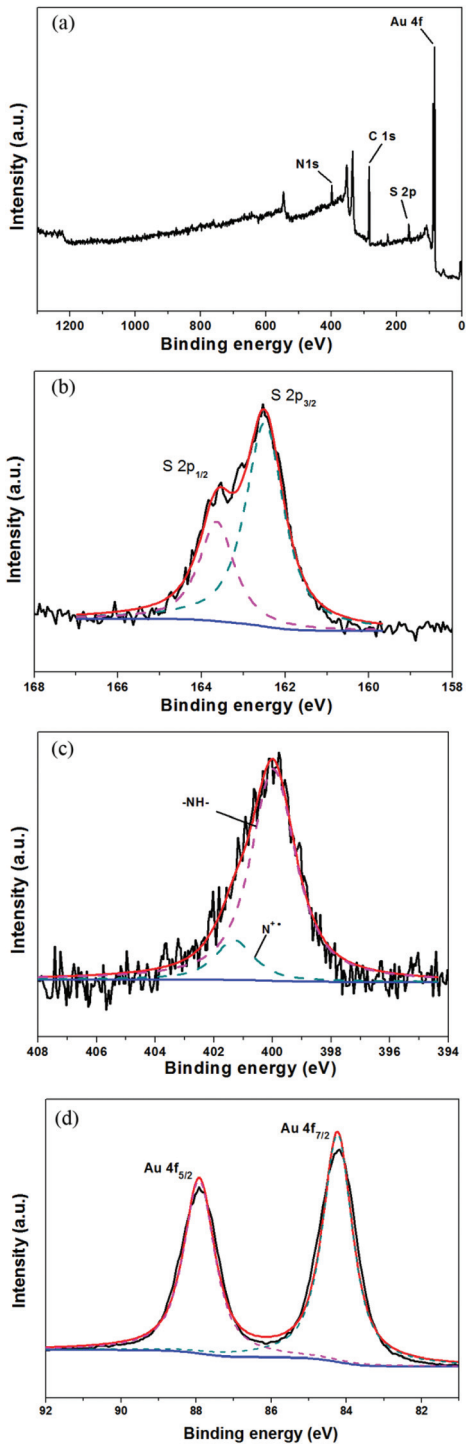

Fig. 2 (a) XPS spectrum of synthesized Au@4-ATP. XPS data for (b) S 2p, (c) N 1s and (d) Au 4f regions of Au@4-ATP.

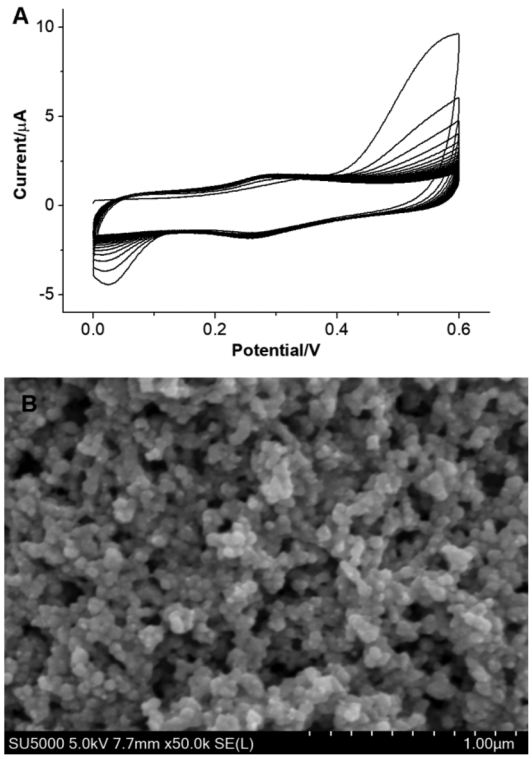

Fig. 3 (A) Electropolymerization curves of AuPP by CV. (B) SEM image of AuPP on Au electrode surface.

the 4-ATP monolayer as a glue layer. During the initial sweeps, a large irreversible oxidation peak was observed at around 0.6 V and the intensity of this peak decreased rapidly as the number of cycles increased; the reduction peak at around 0.024 V had a similar change (as shown in Fig. 3A). This indicated that a polymer film was successfully fabricated on the electrode surface. Additionally, a symmetrical reversible redox wave centered at about 0.26 V attributed to the aromatic amine groups[37,38] was observed in the subsequent sweeps and it attained a steady state in following cycles. This obtained polymer showed electrochemical behavior similar to 4-ATP[37,39,40] and aniline[41] functionalized in other methods, but with a slightly higher current intensity for the redox peak of amine groups. Based on the results, it was envisaged that during the polymerization process, amine groups played a significant role by reacting through different routes[38,41] to link other monomers to form the polymer network. Due to the gold core of the monomer, this polymer was still conductive with a certain electroactivity. This also implied that the characteristics of this polymer were similar to those of MOF materials, which was further verified by the SEM image of the fabricated polymer morphology displayed in Fig. 3B. A uniform and microporous three-dimensional network was easily observed and this favorable structure rendered a higher surface area and more accessible binding sites for further functionalization, key factors for signal amplification. DNA immobilization was achieved by electrochemical deposition as reported previously[42] on the aforementioned AuPP platform. The C–Ag^{+}–C interaction gave rise to abundant preconcentration and introduced dual amplification for final Ag^{+} detection together with the AuPP matrix.

The stepwise construction processes were characterized by CV and electrochemical impedance spectroscopy (EIS),

effective and convenient tools to probe the electron transmission procedure of the modified electrode. As depicted in Fig. 4A, the pair of typical redox peaks of $Fe(CN)_6^{3-/4-}$ decreased to a certain extent when the AuPP film formed on the bare Au electrode surface, indicating that this film was conductive but still affected by the organic ligands. When the DNA was conjugated, an obviously lower response was observed over the potential range due to the formed DNA layer greatly blocking the electron-conducting tunnels in the AuPP. In Fig. 4B, the EIS spectra are represented by Nyquist plots, including a semicircle and a straight linear portion. The semicircle part in the higher frequency region represented the limited process of charge transfer, whereas the linear part in the lower frequency region corresponds to the diffusion-controlled process (Z_w). After the AuPP film was electropolymerized on the electrode surface, the negligible charge transfer resistance (R_{ct} = 57 Ω) in curve a changes to a larger semicircle shape (curve b) as expected, implying an increased but not overly strong (R_{ct} = 1719 Ω) charge transfer resistance to the redox probe. The R_{ct} significantly increased to 7556 Ω (curve c) when the DNA was attached to the AuPP film, which is ascribed to the nonconductive DNA layer hampering electron transfer. This was in accordance with the CV results, further suggesting that the obtained AuPP platform is equipped with admirable properties for sensor construction.

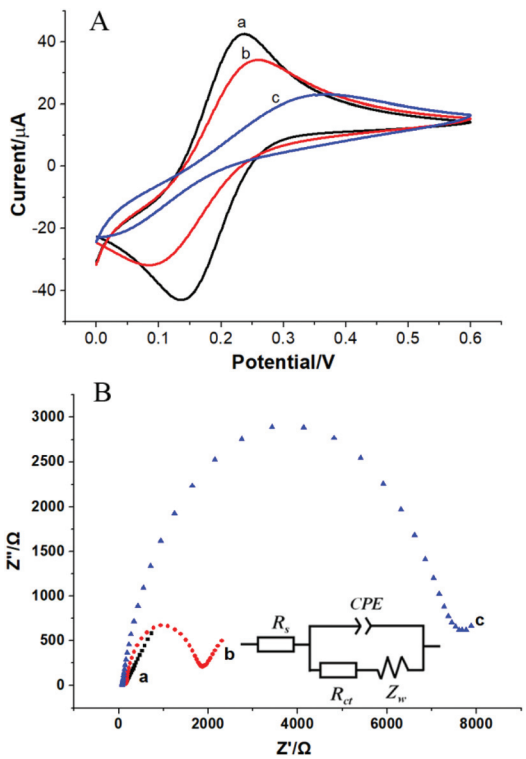

Fig. 4 (A) Cyclic voltammograms and (B) electrochemical impedances of (a) bare Au electrode, (b) AuPP-modified Au electrode (AuPP/Au), and (c) C-riched DNA and MOF-modified Au electrode (DNA/AuPP/Au) in 5 mM $K_3[Fe(CN)_6]/K_4[Fe(CN)_6]$ containing 0.1 mol L^{-1} KCl. Inset: equivalent circuit of EIS.

3.2 Comparison of detection platforms with different modifications

The proposed strategy was to fabricate AuPP as the base and C-riched DNA as the receptor for dual signal amplification. To verify the Ag^+ detection property of the constructed sensor, several electrodes modified through different procedures were compared under the same conditions. As displayed in Fig. 5, the bare Au electrode displayed little electrocatalysis toward 2 μM Ag^+, unlike the carbonaceous electrode. The addition of the AuPP layer slightly improved the signal response of Ag^+, showing a broad and indistinct peak. This implied that the AuPP material itself had limited superiority for the redox reaction or enrichment of Ag^+. When the C-riched ssDNA were directly immobilized on the Au electrode surface, Ag^+ was selectively captured by interaction with cytosine, producing an obvious DPV peak (Fig. 5c). After planting the C-riched DNA on the constructed AuPP matrix, the signal response was enhanced significantly, clearly demonstrating that the combination of AuPP matrix and C–Ag^+–C mismatch had the potential to improve the sensitivity and provide better detection performance for Ag^+.

3.3 Optimization of experimental conditions

For Ag^+ detection, the obtained electrode was first immersed in a supporting electrolyte for electrodeposition to ensure sufficient enrichment of Ag^+ on the electrode surface by specific C–Ag^+–C interaction and then DPV technique was applied to acquire the corresponding current response of Ag^+. Therefore, the factors which might affect the procedure, such as supporting electrolyte, amount of attached DNA on AuPP, and electrodeposition conditions, were explored to achieve the optimal detection performance. Acetate buffer has been widely used as an electrolyte for metal ion detection.[12,43,44] To ascertain whether this electrolyte had the same effect in this system, two other buffer solutions, including nitric acid and citrate, were applied to compare the intensity of the signal. Intriguingly, the result showed that while the acetate buffer had an obvious advantage over citrate, the nitric acid sur-

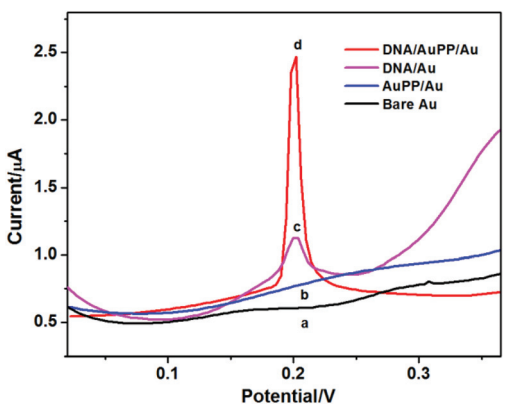

Fig. 5 DPV responses of 2 μM Ag^+ on (a) bare Au electrode, (b) AuPP/Au, (c) DNA/Au and (d) DNA/AuPP/Au.

passed acetate with about 3 times higher current intensity and served as the best supporting electrolyte (Fig. 6A). This phenomenon was explained by the solubilities of the compounds that silver might form in these different solutions.

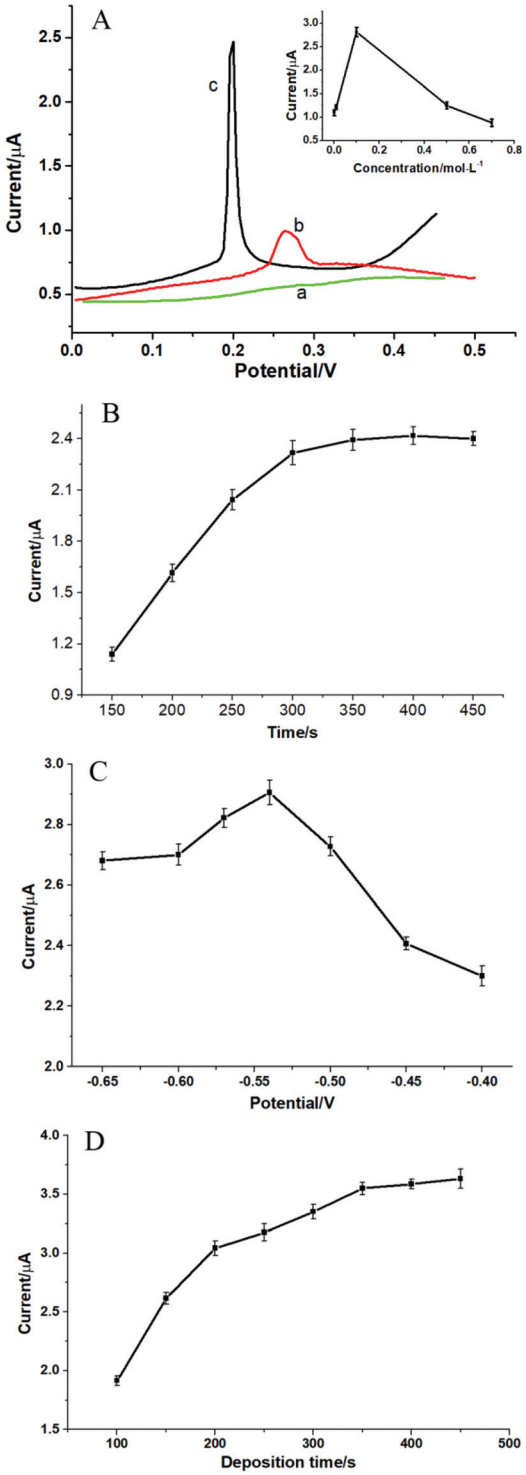

Fig. 6 (A) DPV responses of 2 μM Ag^+ in (a) 0.2 M citrate, (b) 0.2 M acetate, and (c) 0.1 M HNO_3. Inset: effect of HNO_3 concentration on current intensity. Influence of (B) DNA immobilization time, (C) deposition potential and (D) deposition time on signal responses to 2 μM Ag^+.

Silver nitrate has the highest solubility while silver acetate dissolves only slightly in water and silver citrate has the worst solubility of all three. So, the nitric acid system was suitable for the stable existence of Ag^+ and the following detection. The selection of electrolyte concentration, from 0.01 M to 0.7 M, was also carried out. It could be seen clearly in the inset of Fig. 6A that the peak current increased to a maximum when the nitric acid concentration increased from 0.01 to 0.1 M. When the concentration became higher, the too-acidic condition might cause damage to the modifier on the electrode surface, leading to the decrease of the signal.

To take full advantage of the large active surface area supplied by the AuPP layer, it was necessary to consider the loading amount of DNA, which was directly decided by the immobilization time. As exhibited in Fig. 6B, the maximum current was achieved at an immobilization time of 300 s and then the current remained nearly constant, which is attributed to the saturation of DNA on the electrode surface as immobilization time increases. For the deposition conditions of Ag^+ before applying DPV, deposition potential and time were both discussed. Selection of a suitable deposition potential for the preconcentration of Ag^+ is crucial in the DPV technique. Influence of deposition potential was investigated in the range of −0.65 V to −0.4 V and the results are displayed in Fig. 6C. It clearly illustrated that the strongest signal response emerged at the deposition potential of −0.54 V. According to the Nernst equation and the standard electrode potential of Ag^+/Ag (0.799 V), the conditional electrode potential is around 0.268 V taking the activity concentration of Ag^+ as 1 nM, so it was expected that a deposition potential higher than 0.2 V was not sufficient to reduce Ag^+. In practical situations, the applied deposition potential is usually much lower than the calculated theoretical value due to the presence of metal ion coordination with ligands, solvent effect and other influences. When higher than −0.54 V, the potential was not negative enough, while when lower than −0.54 V, the current reduced a little and then remained almost steady. As a result, −0.54 V was considered the optimum deposition potential. Under this potential, more Ag^+ was adsorbed on the electrode surface with prolonged deposition time, giving rise to elevated current intensity. This assumption was in full agreement with Fig. 6D that the current value increased gradually with Ag^+ accumulation till the deposition time was longer than 350s and the electrode surface became saturated. Thus, 350 s was selected as the optimal accumulation time for Ag^+.

3.4 Analysis performance of constructed sensor for silver ion

Under the optimized experimental conditions, the capability of the AuPP and C-rich DNA system for quantitative analysis of Ag^+ was investigated. As depicted in Fig. 7A, the signal intensity of DPV obviously increased with the additional concentration of Ag^+, presenting a good linear calibration plot ranging from 0.005–3 μM (R^2 = 0.993) with a sensitivity of 5.4 μA μM^{-1} cm^{-2}. The detection limit was calculated to be 1.3 nM, which was much lower than the permissible residue limit of Ag^+ in drinking water (0.46 μM). For comparison, character-

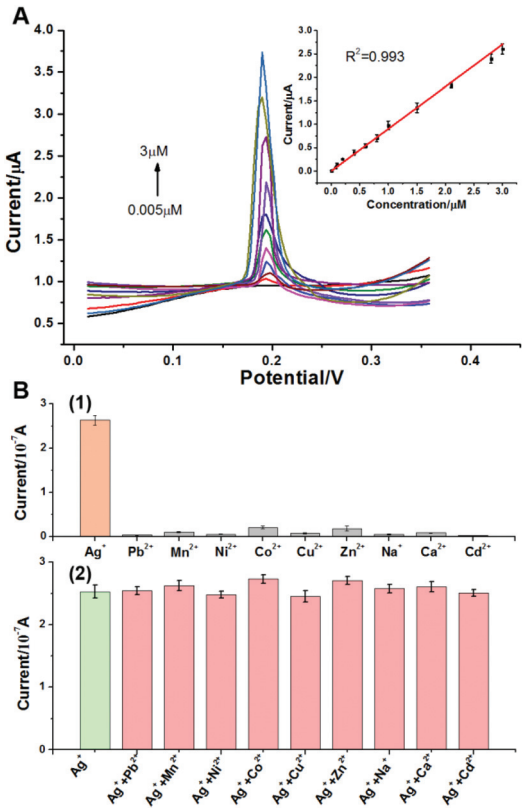

Fig. 7 (A) DPV curves of different concentrations of Ag^+ at 0.005–3 μM on the modified electrode. Inset: the corresponding linear relationship between the current intensity and concentration of Ag^+. (B) Specificity test of 2 μM interference ions without (1) and with (2) 0.2 μM Ag^+.

istics, including linear range and detection limit, reported from other techniques or on other modified electrodes in previous references are summarized in Table 1. Overall, the results proved that this proposed detection strategy had comparable linear dynamic range and an acceptable detection limit, manifesting the admirable applicability of this technique.

The relative standard deviation (RSD) of repeated detection for 1 μM Ag^+ by 4 different modified electrodes was 5.2%. The repeatability of a single DNA/AuPP/Au electrode was also examined through the determination of 1 μM Ag^+ five times and the RSD was calculated as 3.6%, suggesting the favorable reproducibility of the constructed sensor. In addition, the sensor retained 90.2% of its original signal after 7 days of storage at 4 °C, showing its acceptable stability. To evaluate the selectivity of this electrochemical sensor toward Ag^+, interference effects were studied under identical conditions in the presence of other metal ions at 10 times the concentration of 0.2 μM Ag^+, including 2 μM Pb^{2+}, Mn^{2+}, Ni^{2+}, Co^{2+}, Cu^{2+}, Zn^{2+}, Na^+, Ca^{2+}, and Cd^{2+}. These were separately mixed with Ag^+ or existed alone and the current signals of these solutions were determined. Fig. 7B shows that the addition of other metal ions had limited influence on the response of Ag^+, further confirming the selectivity that C–Ag^+–C coordination introduced to the proposed sensor.

Table 1 Comparison of analytical performance of diverse methods for Ag^+ detection

Method	Linear range (μM)	Detection limit (μM)	Ref.
Fluorescence	0–0.4	0.003	19
Fluorescence	0–24	1.2	45
Colorimetry	0.01–0.2	0.0027	17
Colorimetry	0.002–0.005	0.0014	46
Electrochemistry (GaN micropillars)	0.01–1	0.0033	28
Electrochemistry (S-doped graphene and TMB)	50–400	2.15	12
Electrochemistry (AuPP, C–Ag^+–C)	0.005–3	0.0013	This work

Table 2 Detection results of Ag^+ in different water samples

Sample	Original content (10^{-7} M)	Added (10^{-7} M)	Found (10^{-7} M)	Recovery (%)	AAS
Lake water	Not found	0.50	0.537	107.4	0.519
		2.0	2.19	109.5	2.10
Tap water	Not found	0.50	0.489	97.8	0.503
		2.0	2.08	104	2.05

To explore the analytical performance of the constructed electrochemical sensor in practical samples, the Ag^+ concentrations in real water samples, including lake water and tap water, were determined, as well as samples spiked with certain known concentrations of Ag^+. The collected water samples were pretreated simply using a 0.22 μm filtering membrane to remove any suspended materials, followed by centrifugation at 10 000 rpm for 20 min for further purification. The analytical results are listed in Table 2. They showed that no residual Ag^+ was found in either water sample and the recovery of the spiked samples ranged from 97.8%–109.5%. This result was further confirmed by graphite furnace atomic absorption spectrometry (GFAAS), verifying the practicability of this sensing platform for environmental samples.

4. Conclusions

A new platform constructed from Au@4-ATP was introduced for the detection of Ag^+ in coordination with C–Ag^+–C interaction. Based on the definition of MOF, we applied Au NPs as metal centers and an electroactive thiol-functionalized surface protective reagent as ligand to form a 3D porous network, serving as an MOF analogue. This structure supplied the electrode with acceptable conductivity and a large active surface area, increasing the potential for signal enhancement. Additionally, C–Ag^+–C conjugation was applied to achieve detection selectivity, while accumulating the detection target to a certain extent. These two factors endowed the constructed sensor with admirable detection sensitivity and selectivity, a detection limit of 1.3 nM and anti-interference to other metal

ions. This proposed strategy might open a new perspective on exploring possible functions and materials by applying Au NPs functionalized with designed ligands. Furthermore, other metal nanomaterials in various morphologies could also be considered as powerful candidates, leading to broad application potential.

Conflicts of interest

There are no conflicts to declare.

Acknowledgements

This work was supported by the National Natural Science Foundation of China (21765005), Guangxi Natural Science Foundation (2018GXNSFAA138047), Science and Technology Project of Guangxi (GuikeAD19110096).

References

1 K. Jeeva, M. Thiyagarajan, V. Elangovan, N. Geetha, *et al.*, *Ind. Crops Prod.*, 2014, **52**, 714.
2 M. E. Samberg, P. E. Orndorff and N. A. Monteiro-Riviere, *Nanotoxicology*, 2011, **5**, 244.
3 S. Chernousova and M. Epple, *Angew. Chem., Int. Ed.*, 2013, **52**, 1636.
4 P. Christopher, H. Xin and S. Linic, *Nat. Chem.*, 2011, **3**, 467.
5 C. Marambio-Jones and E. M. V. Hoek, *J. Nanopart. Res.*, 2010, **12**, 1531.
6 S. W. P. Wijnhoven, W. J. G. M. Peijnenburg, C. A. Herberts, W. I. Hagens, *et al.*, *Nanotoxicology*, 2009, **3**, 109.
7 E. Navarro, F. Piccapietra, B. Wagner, F. Marconi, *et al.*, *Environ. Sci. Technol.*, 2008, **42**, 8959.
8 H. T. Ratte, *Environ. Toxicol. Chem.*, 1999, **18**, 89.
9 A. H. Pakiari and Z. Jamshidi, *J. Phys. Chem. A*, 2010, **114**, 9212.
10 N. B. Luque and E. Santos, *Langmuir*, 2012, **28**, 11472.
11 L. Fu, A. Wang, K. Xie, J. Zhu, *et al.*, *Sens. Actuators, B*, 2020, **304**, 127390.
12 Y. Fu, Y. Yang, T. Tuersun, Y. Yu, *et al.*, *Analyst*, 2018, **143**, 2076.
13 H. Wang, Q. Lu, M. Li, H. Li, *et al.*, *Anal. Chim. Acta*, 2018, **1027**, 121.
14 A. Ono, S. Cao, H. Togashi, M. Tashiro, *et al.*, *Chem. Commun.*, 2008, **39**, 4825.
15 P. Miao, Y. Tang and L. Wang, *ACS Appl. Mater. Interfaces*, 2017, **9**, 3940.
16 H. Gong and X. Li, *Analyst*, 2011, **136**, 2242.
17 B. W. Liu, Y. Y. Wu, P. C. Huang and F. Y. Wu, *Microchim. Acta*, 2019, **186**, 467.
18 Y. Wen, F. Xing, S. He, S. Song, *et al.*, *Chem. Commun.*, 2010, **46**, 2596.
19 W. Zhou, J. Ding and J. Liu, *Biosens. Bioelectron.*, 2017, **87**, 171.
20 K. Feng, Y. Kang, J. J. Zhao, Y. L. Liu, *et al.*, *Anal. Biochem.*, 2008, **378**, 38.
21 P. Miao, L. Ning and X. Li, *Anal. Chem.*, 2013, **85**, 7966–7970.
22 G. Zhu and C. Y. Zhang, *Analyst*, 2014, **139**, 6326.
23 J. Sun, Y. Gan, T. Liang, S. Zhou, *et al.*, *Curr. Opin. Electrochem.*, 2019, **17**, 23.
24 Z. P. Chen, Z. F. Peng, Y. Luo, B. Qu, *et al.*, *Biosens. Bioelectron.*, 2007, **23**, 485.
25 X. F. Qin, Y. P. Lu, M. M. Bian, Z. R. Xiao, Y. Zhang and Y. L. Yuan, *Anal. Chim. Acta*, 2019, **1091**, 119.
26 C. Kokkinos, *Nanomaterials*, 2019, **9**, 1361.
27 Q. Liu, J. Li, W. Yang, X. Zhang, *et al.*, *Anal. Chim. Acta*, 2020, **1100**, 22–30.
28 P. Sidambaram and J. Colleran, *J. Electrochem. Soc.*, 2019, **166**, B532.
29 S. Ansari, M. S. Ansari, H. Devnani, S. P. Satsangee, *et al.*, *Sens. Actuators, B*, 2018, **273**, 1226.
30 Y. Wang, D. Fan, G. Zhao, J. Feng, *et al.*, *Biosens. Bioelectron.*, 2018, **120**, 1.
31 Z. Z. Guo, A. Florea, C. Cristea, F. Bessueille, *et al.*, *Sens. Actuators, B*, 2015, **207**, 960.
32 P. J. Debouttière, S. Roux, F. Vocanson, C. Billotey, *et al.*, *Adv. Funct. Mater.*, 2006, **16**, 2330.
33 J. E. Hutchison, T. A. Postlethwaite and R. W. Murray, *Langmuir*, 1993, **9**, 3277.
34 M. Wirde and U. Gelius, *Langmuir*, 1999, **15**, 6370.
35 X. M. Feng, R. M. Li, Y. W. Ma, R. F. Chen, N. E. Shi and W. Huang, *Adv. Funct. Mater.*, 2011, **21**, 2989.
36 Y. Negishi, K. Nobusada and T. Tsukuda, *J. Am. Chem. Soc.*, 2005, **127**, 5261.
37 C. R. Raj, F. Kitamura and T. Ohsaka, *Langmuir*, 2001, **17**, 7378.
38 J. Liansheng, L. Niu, J. Shen, T. You, *et al.*, *Electrochem. Commun.*, 2005, **7**, 219.
39 M. Yola and N. Atar, *Electrochim. Acta*, 2014, **119**, 24.
40 L. Feng, W. Chen, P. Dong and S. Zhang, *Biosens. Bioelectron.*, 2009, **24**, 2160.
41 E. Granot, F. Patolsky and I. Willner, *J. Phys. Chem. B*, 2004, **108**, 5875.
42 H. R. A. Hasanjani and K. Zarei, *Biosens. Bioelectron.*, 2019, **128**, 1.
43 X. Zhu, Y. Yuan, Y. Zhang, J. Li, *et al.*, *Electroanalysis*, 2018, **30**, 1715.
44 Y. L. Yuan, G. M. Pang, X. K. Li, W. Y. Zhu, *et al.*, *Anal. Methods*, 2017, **9**, 5586.
45 F. Ye, X. M. Liang, K. X. Xu, X. X. Pang, *et al.*, *Talanta*, 2019, **200**, 494.
46 C. R. Li, J. Hai, L. Fan, S. L. Li, *et al.*, *Sens. Actuators, B*, 2019, **284**, 213.

